GUPTA, R., PANCHOLI, P.V., YU, X., GUPTA, L., STENNING, G.B.G., BUCKNALL, D., FLYNN, D. and PANCHOLI, K. 2023.
Role of interface in optimisation of polyamide-6/Fe3O4 nanocomposite properties suitable for induction heating.
Nano-structures and nano-objects [online], 34, article number 100973. Available from:
https://doi.org/10.1016/j.nanoso.2023.100973

Role of interface in optimisation of polyamide-6/Fe3O4 nanocomposite properties suitable for induction heating.

GUPTA, R., PANCHOLI, P.V., YU, X., GUPTA, L., STENNING, G.B.G., BUCKNALL, D., FLYNN, D. and PANCHOLI, K.

2023

Nano-Structures & Nano-Objects 34 (2023) 100973

Contents lists available at ScienceDirect

Nano-Structures & Nano-Objects

journal homepage: www.elsevier.com/locate/nanoso

Role of interface in optimisation of polyamide-6/Fe_3O_4 nanocomposite properties suitable for induction heating

Ranjeetkumar Gupta [a,*], Pinakin V. Pancholi [g], Xiangyan Yu [b], Lakhan Gupta [h], Gavin B.G. Stenning [c], David Bucknall [d], David Flynn [e], Ketan Pancholi [a,f,**]

[a] School of Engineering, Robert Gordon University, Aberdeen AB10 7GJ, UK
[b] School of Engineering and Materials Science, Queen Mary University of London, Mile End Road, London, E1 4NS, UK
[c] ISIS Neutron and Muon Source, STFC Rutherford Appleton Laboratory, Didcot OX11 0QX, UK
[d] Institute of Chemical Sciences, School of Engineering & Physical Sciences, Heriot-Watt University, Edinburgh EH14 4AS, UK
[e] James Watt School of Engineering, University of Glasgow, Glasgow G12 8QQ, UK
[f] Advanced Materials Group, School of Engineering, Robert Gordon University, Aberdeen, AB10 7GJ, UK
[g] Chemistry Department, Gujarat College, Ahmedabad, Gujarat, 380006, India
[h] Quality and Assurances Department, Krishna Enterprises, Sector-69, HSIIDC IMT, Faridabad 121004, India

ARTICLE INFO

Article history:
Received 9 August 2022
Received in revised form 21 February 2023
Accepted 4 April 2023

Keywords:
Nanocomposites
Thermoplastic
In-situ polymerisation
Silica
Stöber
Crystallinity

ABSTRACT

Induction heating of magnetic nanoparticles (MNPs) and localised melting of the surrounding high temperature engineering polymer matrix by generating microscopic or macroscopic eddy currents during magnetisation of a polymer nanocomposite (PMC) is crucial for realising induction heating aided structural bonding. However, the polymer heating should be homogeneous and efficient to avoid local pyrolysis of the polymer matrix, which results in degraded mechanical properties, or requiring a large coil for generating a high frequency magnetic field. Increasing the interfacial area by homogeneously dispersing the MNPs in the polymer matrix provides many microscopic eddy currents to dissipate the power through magnetisation and polarisation, leading to micro eddy current induced uniform heating of the PMC. However, the application of a hydrophobic coating on MNPs to aid dispersion can perturb the generation of eddy currents and affect the crystallinity and size of the crystallites responsible for the mechanical properties. In this work, the dielectric and magnetic properties, as well as the degree/size of crystallinity of a PMC containing oleic acid (OA) (22 and 55 w/w%) and silica coated (Stöber and reverse emulsion method) Fe_3O_4 MNPs were measured to evaluate the effect of the interfacial coating and its chemistry. The correlation between the measured properties and dispersion state of the MNPs was established to demonstrate the comprehensive effects of interfacial coating on the PMC and this is a unique method to select a suitable PMC for induction aided structural bonding applications. The results showed that the lower amount of OA (22 w/w%) helped achieve the best dispersion to reduce the crystallinity size and increase degree of crystallinity, and to give the best candidate for achieving mechanical properties of the bonded carbon fibre reinforced polymer (CFRP). Moreover, the low concentration of OA helped achieve high polarisation for dielectric heating as well as eddy current formation due to the relatively high magnetic saturation. The silica coating proportionally reduced the magnetic response and electric polarisation of the PMC, which could affect its eddy current generation that is responsible for induction heating.

1. Introduction

Magnetic polymer materials or magnetic nanoparticles can potentially be used in many applications, such as drug delivery, biosensing, catalysis, bio-separation, data storage, switch mode power supplies [1] and medical imaging [1a]. Adding magnetic nanoparticles (MNP) such as iron(II, III) oxide (Fe_3O_4) or ferric/iron(III) oxide (Fe_2O_3) into the polymer imparts magnetic properties to the entire PMC [2]. When a PMC is exposed to an alternating magnetic field, it will induce heat in the polymer, which is a

---

[*] Correspondence to: Engineering Development - Process Modelling, National Composites Centre, Bristol & Bath Science Park, Emersons Green, Bristol BS16 7FS, UK.

[**] Corresponding author at: School of Engineering, Robert Gordon University, Aberdeen AB10 7GJ, UK.

E-mail addresses: ranjeetkumar.gupta@nccuk.com (R. Gupta), k.pancholi2@rgu.ac.uk (K. Pancholi).

https://doi.org/10.1016/j.nanoso.2023.100973

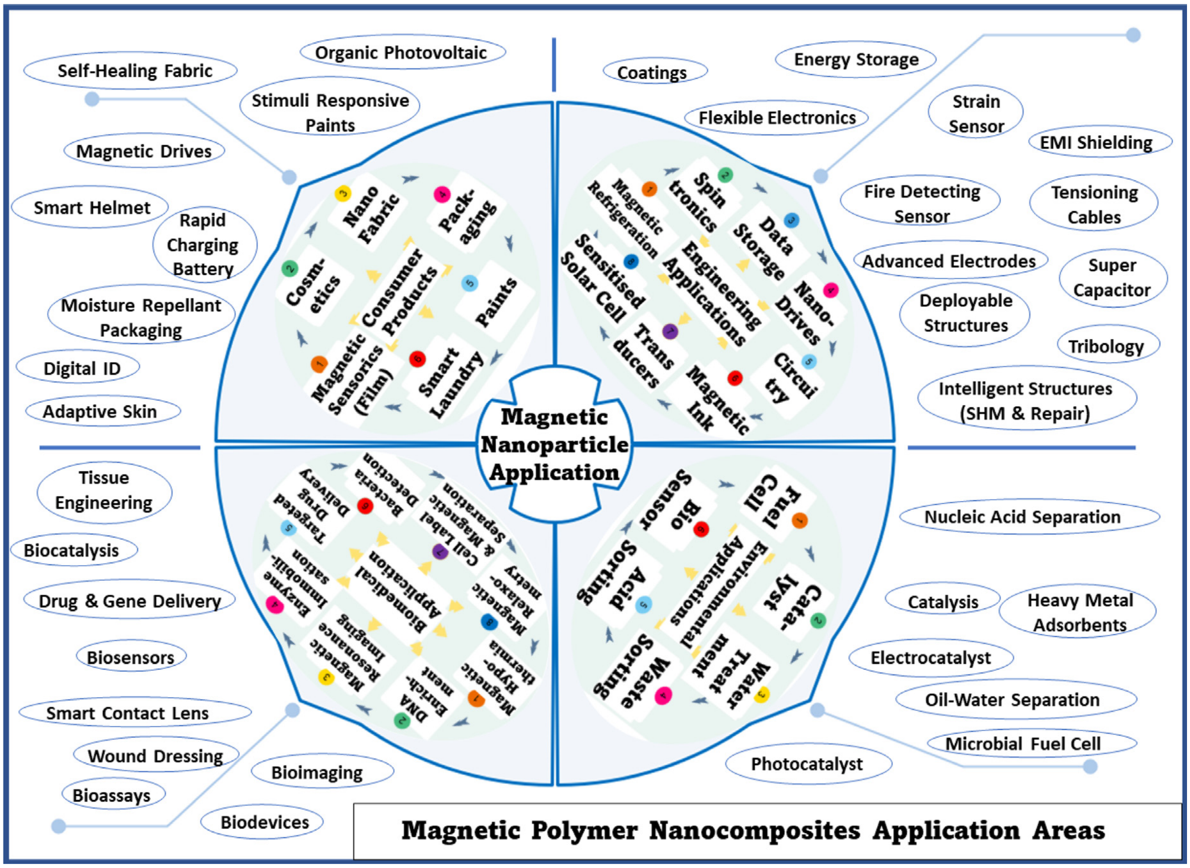

Fig. 1. Graphical overview of the four thematic application areas of magnetic nanoparticles and their synthesised polymer magnetic nanocomposites.

useful property in many applications, such as protective coatings that can self-heal, thermal welding and magnetic hypothermia. The main thematic magnetic nanoparticle and magnetic polymer applications can be divided into four major application areas, as summarised in Fig. 1.

The inductive heating of a PMC is performed by applying a time-varying magnetic field using an inductive coil, which is supplied with an electric current via a high-power alternating voltage. The generated alternative magnetic field has the same frequency as the frequency of electric current and voltage. Induction heating of a PMC involves two different primary mechanisms: eddy currents and joule heating [3]. The joule heating mechanism only takes place when a network of MNPs is established within the polymer. Moreover, the heat power dissipation through joule heating is far smaller than that from eddy current loops formation at the macroscale.

The eddy currents in a PMC form at multiple scales (macro and micro) via magnetic domain interaction and magnetic field diffusion, respectively. The macroscopic or global eddy current loops form at the interface between adjacently located conductive MNPs, whereas the microscopic eddy current forms at the interface between the individual MNP and the polymer matrix due to their polarisation, which follows Faraday's law [4]. If the MNPs are well dispersed and do not form a network, the micro eddy current is generated. In the case of well dispersed MNPs, generating ferroelectric materials, the micro eddy current as well as the magnetisation polarisation reversal contribute to heat generation, however, the magnetisation hysteresis curve following the Neel relaxation, where the reversal of the spin of magnetic moment for each domain takes place, does not contribute significantly to the heat produced [5]. Generation of heat through magnetisation only takes place when the temperature is below the Curie point; above this temperature the nanoparticles lose their ferromagnetic properties. The efficiency of both effects are dependent on the ferroelectric and magnetic properties of the PMC [6].

Another important aspect is the frequency of the applied external magnetic field. A higher frequency limits the penetration depth of the field. The penetration depth is directly proportional to the electrical resistivity, but inversely proportional to the magnetic permeability and frequency. Many metals and their alloys display high magnetic saturation and permeability, however, heating through the eddy current mechanism depends on the conductivity of those metals within the polymer matrix and the ability for penetration in the PMC

A precondition of achieving both properties in a PMC is to disperse the MNPs homogeneously within the polymer matrix and to control the distance between MNP clusters, so as to establish a single domain structure for enhanced magnetic saturation. However, the processing parameters and input materials need to be controlled to achieve the homogeneous dispersion; namely the MNP loading, coating, types of polymers and mixing method. For example, increasing the MNP loading reduces the inter-particle distances, with the formation of agglomerates due to short range Van der Waals or hydrogen bonds. Similarly, the presence of an interface between solid–gas–liquid in a nanocomposite can also enhance the agglomeration of nanoparticles [7,8]. It is a significant challenge to avoid the formation of MNP agglomerates in a polymer matrix as the agglomerations can cause an uneven response to an applied external magnetic field due to melting excessively or undergoing pyrolysis [9]. To avoid agglomeration formation, many researchers have used ultrasonication [10], curing temperature adjustment [11] and suitable MNP surface modification [12].

The level of the interactions and bonding strength between phases are vital in determining the dispersion of MNPs in a polymer matrix. Hence coating the MNP surfaces using ionic charge, polymer coating (brushes), small molecules and core–shell arrangement for creating a designed coating is more efficient way to promote dispersion in the hydrophobic polymer through an electrostatic or steric mechanism [13]. These techniques enhance the polymer–nanocomposite interactions at the nanoscale to avoid formation of agglomerates. Many studies have analysed the effect of the MNP coating on its adhesion with the polymer matrix [14–17]. The in-situ polymerisation method is widely used for preparing a polyamide nanocomposite [18] as the low viscosity monomer allows a uniform dispersion of the MNPs and promotes covalent bonding between the polymer matrix and the MNP coating surfaces [14].

However, the introduction of the surface coating on the MNPs creates two interfaces: one with the outer polymer matrix and another with the MNP. Existence of a thin coating of dissimilar magnetic permittivity on the MNP interferes with the magnetic field continuity along the interface and reduces space charge generation on the conducting surface of the MNP which, in turn, affects the macroscale magnetic properties and polarisation [19]. Additionally, the chemical structure of the coating material and dispersion state will affect the space current and charge density. This research reports the effects of variable concentrations of the silica and oleic acid (OA) coating on the magnetic properties and polarisation of Fe_3O_4 nanoparticles and the polymer magnetic nanocomposites (PMC) prepared using these coated MNPs. The effect on the glass transition temperature, peak melting temperature, interaction radius and degree of crystallinity of the PMC samples prepared by in-situ anionic PA6 polymerisation was also investigated to understand the mechanism behind the changes in the magnetic properties and polarisation of the MNPs in PMC.

The interaction radius, a measure of describing the dispersion state using the correlation between the agglomerate size and distance between them, was derived and validated using small angle and wide-angle X-ray scattering, along with a simulated 3D model representing the PMC sample. Finally, all the results were correlated with the magnetic and polarisation response data for assessing the PMC sample with the superior dispersion state, highest degree of crystallinity and optimised magnetic response. Such PMC property and magnetic behaviour tuning can be utilised for a bespoke response, for example the magnetic nature of the PMC can be exploited as a melt response under an induced electromagnetic (EM) field with remotely targeted EM waves or even microwaves. Such a response of a designed PMC can be usefully involved in remotely controlled stimuli induced melt flow for limiting crack propagation or even delaying damage in composite structures or stimuli based structural monitoring.

2. Experimental section

2.1. Materials

ε-Caprolactam (CLm) (99% purity), 3.0 M ethyl magnesium bromide (EtMgBr) solution in diethyl ether, N-acetyl caprolactam (NACL) (99% purity), iron(III) oxide MNPs (<50 nm particle size), (3-aminopropyl)triethoxysilane (APTES) (99% purity) and Span-85 were purchased from Sigma-Aldrich Company Ltd. Dorset, UK, and used as received. The deionised water with 18 MO conductivity was used throughout the experiments. Other laboratory agents were used as standard. All nanoparticles were heated to above 230 °C in air before coating to remove moisture and make them free flowing.

2.2. Experimental methods

i. Stöber functionalisation method

The as-received iron(III) oxide MNPs, weighing 2.0 g, were added to 65 mL of an aqueous citric acid (0.5 g/mL concentration) solution while stirring. For effective adsorption, the pH value was adjusted to 5.2 by adding an aqueous ammonia solution, which resulted in dissociation of two carboxylic groups from each of the citric acid molecules. Further adsorption was enhanced by heating to 80 °C with rigorous stirring for 90 min. Subsequently, the pH was increased to 10.1, wherein the third carboxylic group of the adsorbed citric acid was dissociated [20]. The resulting nanoparticles have a higher surface charge, aiding electrostatic inter-particle repulsion and preventing agglomeration.

The Stöber coating method steps, included the first hydrolysis and then polycondensation, are based on deposition of Tetraethyl orthosilicate (TEOS) [21]. Firstly, 0.85 g of the TEOS solution in ethanol were added to the prepared aqueous suspension of the iron(III) oxide MNPs to maintain a mass ratio of MNP to TEOS of 2.4. The average diameter of the coated MNPs was considered to be 30 nm. The pH was then stabilised at 12.0 by adding aqueous NH_3, enabling the Stöber reaction. The resulting mixture was sonicated for 3 h using a probe-type 150-Watt sonicator (Soniprep 150; MSE., UK), while maintaining the solution at room temperature (RT). Subsequently, the MNPs were centrifuged at 5000 rpm for 5 min and then washed thoroughly three times with DI water. The collected MNPs were dried in oven at 120 °C under vacuum and further sieved. The summary of the processing technique is presented in Fig. 2.

ii. Tri-phasic reverse emulsion coating (TPRE) method

Silica coated MNPs were synthesised following the standard Stöber method [22], then 150 mg of silica coated MNPs were added into the 30 ml toluene and 5 gm span-85 mixture. A tri-phasic reverse emulsion was then formed by shaking. APTES was introduced to make up the final concentration of 2% w/v and then mixture was placed in oil bath at 50 °C for 5 h with continuous stirring.

Decantation was used to separate the MNPs and then they were washed three times with 0.8% (v/v) glacial acetic acid in a dry methanol coupling solution, and kept in the same solution at RT. A summary of the processing technique is presented in Fig. 3.

iii. Oleic acid functionalisation method

The Fe_3O_4 (iron(III) oxide) MNPs were taken in two batches of 0.225 g each and dispersed in 10 ml of methanol. Subsequently, OA was added to each individual batch to make up 22 and 55% w/w solutions. The resulting solution was then mixed thoroughly using a probe type sonicator (150 Watts for 10 min). After an hour, the mixture was centrifuged at 3500 rpm for 8 min and the supernatant was decanted. To the remaining MNPs, fresh methanol in amount equivalent to the discarded supernatant was added and the cycle of ultrasonication and centrifugation was triplicated to remove excess OA. Finally, the MNPs were filtered using filter paper no.1 and washed with deionised water. The MNPs were dried overnight in an oven at 50 °C under vacuum. A summary of the processing technique is presented in Fig. 4.

iv. In situ synthesis of magnetic polymer (PA6-polyamide-6) (PMC)

The in-situ synthesis of PMC involves the polymerisation of the liquid monomer ε-caprolactam (CLm) and a magnetic nanoparticle suspension. To prepare the PMC [23], firstly, 1 wt% coated (functionalised) iron oxide nanoparticles were added to 30 g CLm at 60 °C in an inert nitrogen environment. Subsequently, the MNPs and monomer mixture was sonicated for 30 min at 20 kHz for efficient MNP dispersion. The temperature of the mixture was increased to 150 °C and then 0.86 mL EtMgBr (at 2.5 mol% mol^{-1} CLm concentration) was added in an inert gas environment. Polymerisation was completed by adding 0.94 mL NACL (2.5 mol.%) at 160 °C [23–25]. The mixture polymerised instantaneously and retained the MNP dispersion. The

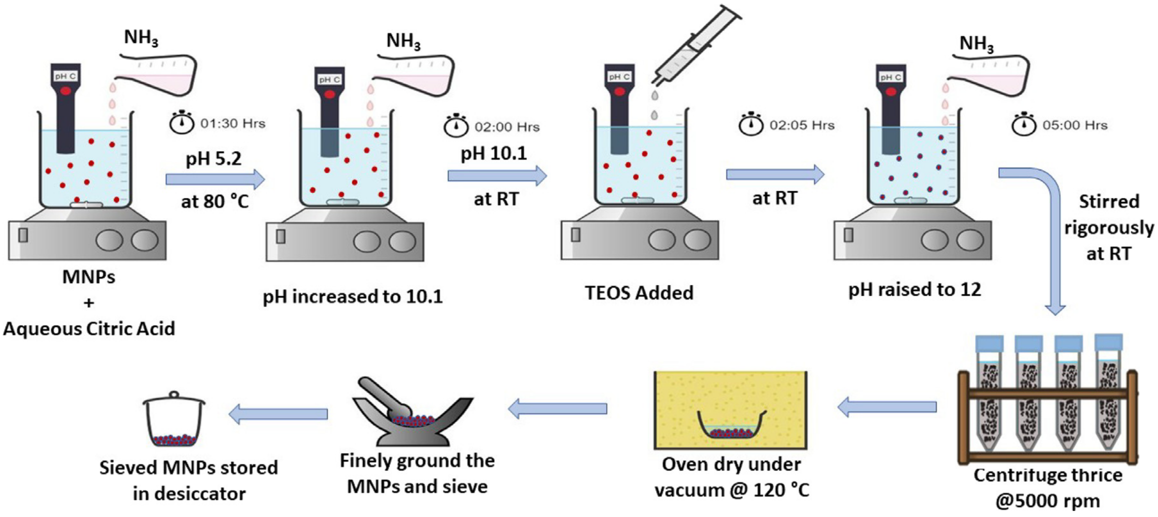

Fig. 2. Experimental procedure that was followed for the Stöber method of coating the MNPs.

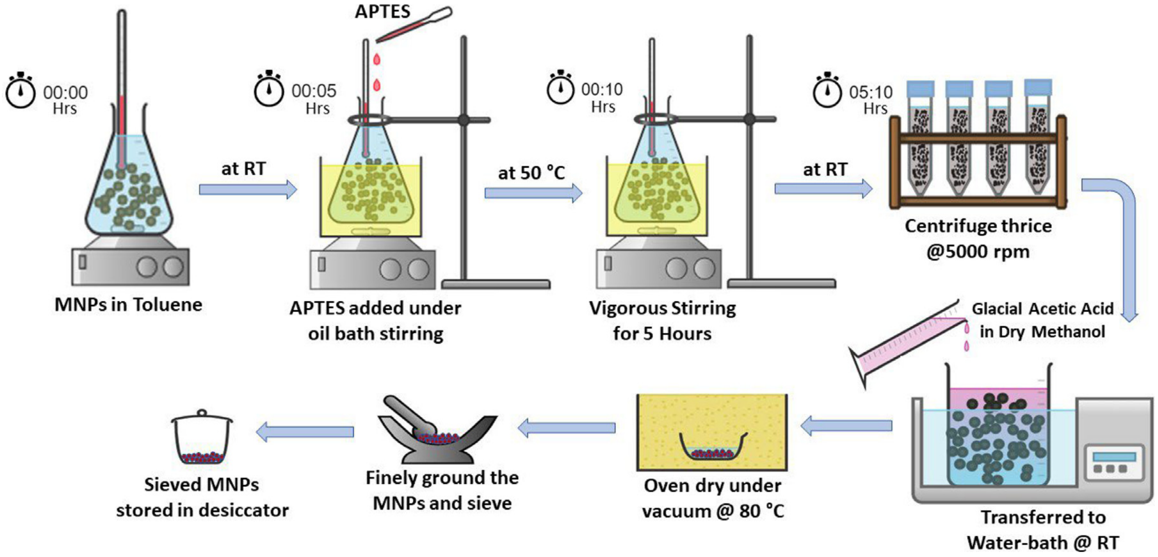

Fig. 3. Experimental procedure that was followed for the TPRE coating of MNPs.

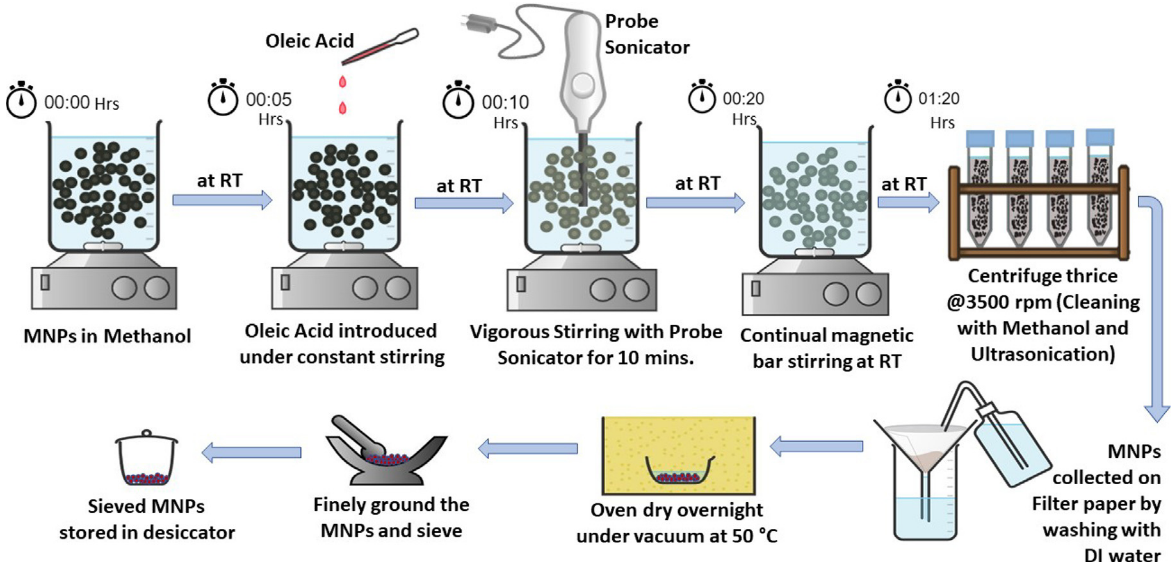

Fig. 4. Experimental procedure that was followed for the oleic acid (OA) coating of MNPs.

Table 1
Prepared samples for this study are summarised herein.

Sample description	Silica loading	Oleic acid loading	MNPs wt% loading in PMC	Here onwards referred in the manuscript as
Uncoated MNPs	0	0	n/a	Uncoated-Fe_3O_4 MNPs
Stöber method functionalised MNPs	Stöber method – low silica content	n/a	n/a	Stöber-Fe_3O_4 MNPs
TPRE method functionalised MNPs	TPRE method – high silica content	n/a	n/a	TPRE-Fe_3O_4 MNPs
22 w/w% Oleic acid functionalised MNPs	n/a	22 w/w% on MNPs	n/a	22 w/w% OA-Fe_3O_4 MNPs
55 w/w% Oleic acid functionalised MNPs	n/a	55 w/w%	n/a	55 w/w% OA-Fe_3O_4 MNPs
Pristine PA6 polymer	n/a	n/a	0	Pristine PA6
PMC prepared with no coating applied to MNPs	0	0	1	Uncoated-Fe_3O_4 PMC
PMC prepared with the Stöber method functionalised MNPs	Stöber method – low silica content	n/a	1	Stöber-Fe_3O_4 PMC
PMC prepared with the TPRE method functionalised MNPs	TPRE method – high silica content	n/a	1	TPRE-Fe_3O_4 PMC
PMC prepared with 22 w/w% oleic acid functionalised MNPs	n/a	22 w/w% on MNPs	1	22 w/w% OA-Fe_3O_4 PMC
PMC prepared with 55 w/w% oleic acid functionalised MNPs	n/a	55 w/w% on MNPs	1	55 w/w% OA-Fe_3O_4 PMC

nanocomposites were washed with deionised water (18 MΩ cm) at 100 °C thoroughly before characterisation, to eliminate any unreacted monomer, initiator or activator. The prepared samples for characterisation are listed in Table 1.

All the prepared samples were characterised using various methods, which are detailed within the Supplementary Data, with the results discussed in Section 3.

3. Results and discussion

3.1. Size distribution and magnetic properties of the coated MNPs

Fig. 5(a), (b), (c), (d) and (e) show the TEM micrographs of all the MNPs. The average agglomerate size of uncoated iron oxide MNPs derived from the TEM images were found to be in range of 35–50 nm, whilst size of the MNP agglomerates for the MNPs coated using the Stöber method were in the range of 30–60 nm. The MNP agglomerate sizes coated using the TPRE method were in range of 30–50 nm while the 22 and 55% oleic acid coated MNP agglomerate sizes were in range of 25–40 and 30–60 nm, respective. The thickness of the silica layer on the Stöber and TPRE functionalised MNPs were found to be *ca.* 2–3 and 7–9 nm, respectively, whilst the thickness of the formed OA layer on the MNP surfaces was *ca.* 2–4 and 6–10 nm for 22 and 55 w/w% OA loading, respectively. The adsorption of OA on the MNPs surface was less transparent to the electron beam and therefore the coating on the MNPs was observed as a thick opaque layer.

The magnetic properties of the iron oxide MNPs and PMC samples, as mentioned in Table 1, were obtained from their magnetic moment-applied magnetic field (M-H) curve responses at 100 and 400 K (characterisation methodology in the Supplementary Data). The M-H loops display the ferrimagnetic behaviour of the material, however, the variation in saturation values due to the silica and oleic acid coatings is clearly distinguishable in Fig. 5(f) and (g), though the MNPs were uniformly magnetised in the remanent state; termed as a single domain state. As seen in Table S2, Appendix A in the Supporting Data (full scale plots included in the Supporting Data S4), the ratios (M_r/M_s) (remanence magnetisation (M_r) to saturation magnetisation (M_s)) were found to be <0.4 for all coated and uncoated MNPs. As the temperature was increased to 400 K, the ratio values fell further to a maximum of 0.24 (22 w/w% OA-Fe_3O_4 MNPs), confirming the incoherent reversal of the magnetic moments. However, the interaction between the MNPs led to alignment and incoherent magnetic moment rotations, which was manifested in lower ratio values. The key measured responses at 100 and 400 K are summarised in Tables S4 and S5, Appendix A in Supporting Data, respectively.

The combination of higher coercivity with a smaller magnetic moment ratio is suitable for having a higher superparamagnetic response, but with a lower magnetic remanence and higher magnetic saturation. With this observation the uncoated-Fe_3O_4 MNPs and TPRE-Fe_3O_4 MNPs were suitable candidates, though the TPRE- Fe_3O_4 MNPs showed quite a low moment ratio compared to all the other samples. Here, the drop in the magnetic remanence was observed with the presence and increased silica coating on the MNPs, which were suppressing the magnetic response due to the low magnetic permittivity silica layer formation. The thick silica layer in the case of TPRE-Fe_3O_4 MNPs, reduced their magnetic saturation values. Overall, the 22 w/w% OA-Fe_3O_4 MNPs gave the highest magnetic saturation of 6715 $\times$ 10^{-4} emu/g at 400 K, which is close to magnetic saturation value of 6512 $\times$ 10^{-4} emu/g for the Stöber-Fe_3O_4 MNPs at 400 K. Conversely, the magnetic saturation was found to be highest for the Stöber-Fe_3O_4 MNPs at 100 K, compared to 22 w/w% OA-Fe_3O_4 MNPs. This observation explains the role of a higher temperature in reducing the dipole and magnetic interactions between the oleic acid coated MNPs. The ability of the coating to promote agglomeration and the thickness determines the overall magnetic response of the MNPs. To evaluate the magnetic and dielectric properties of the PMC due to incorporation of these nanoparticles, the dispersion state and crystallinity were determined.

The low magnetisation of the uncoated-Fe_3O_4 MNPs is due to the pre-heating of the nanoparticles before coating. Since all the uncoated-Fe_3O_4 MNPs were heated to above 230 °C in air before coating, their conversion to α-Fe_2O_3, a weak magnetic phase, is reduced along with any carbon impurities. The XRD plot and discussion with regards to the low saturation magnetisation is give in the Supplementary Data, section S6.

3.2. Functional group analysis of PMC

The presence of the coatings and MNPs was verified by observing the FTIR spectra of the PMC samples (Fig. 6(a))

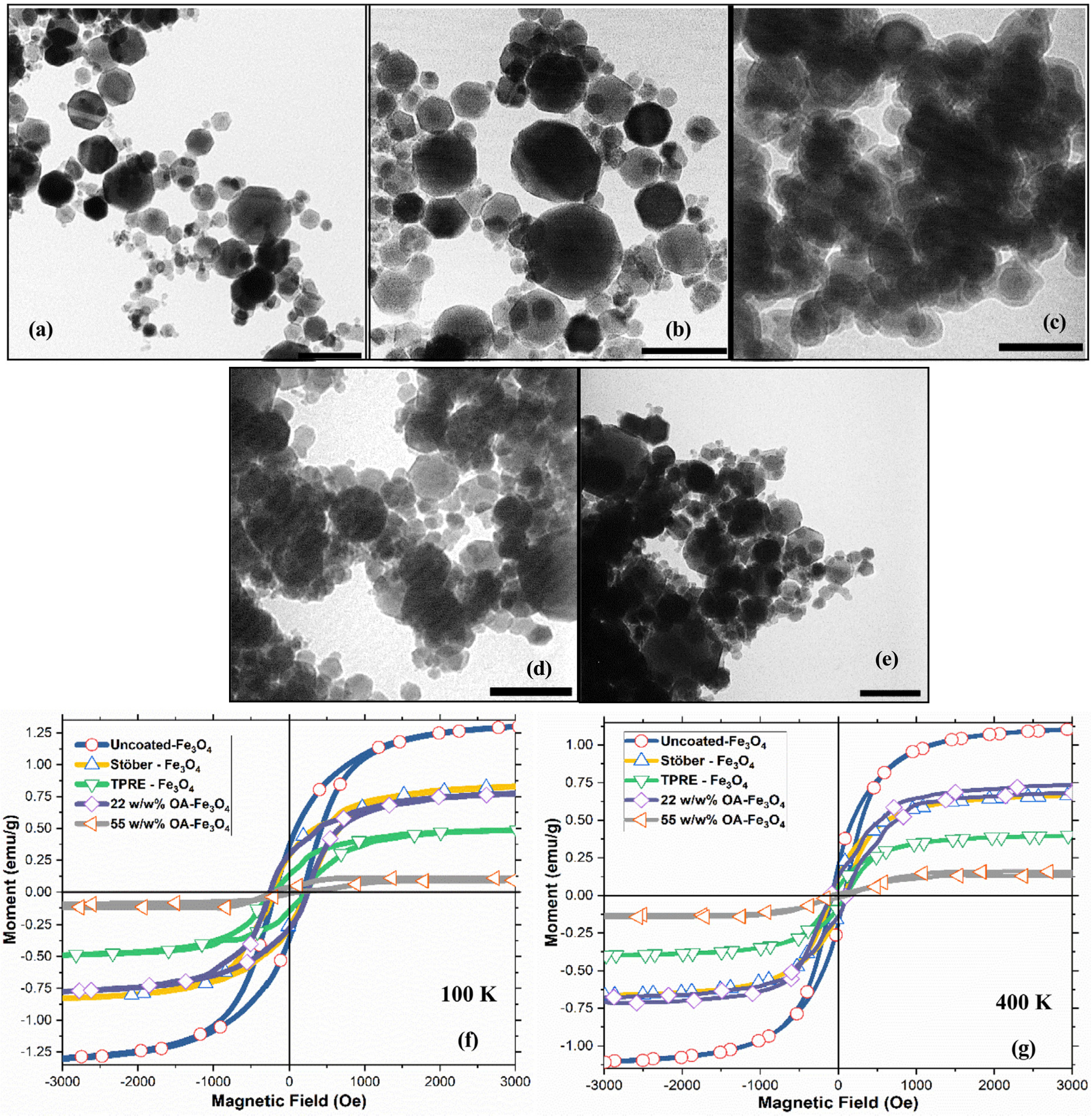

Fig. 5. (a) A representative TEM micrograph showing uncoated MNPs; (b) and (c) represent the TEM micrographs of MNPs with silica coating applied using Stöber and TPRE methods respectively; (d) and (e) show the TEM micrographs of MNP samples with 22 and 55 w/w% OA coating, respectively (scale bar shown for all TEM micrograph is of 100 nm); (f) and (g) magnetisation hysteresis loops for all MNP samples at 100 and 400 K, respectively.

containing MNPs with different coatings. As observed in Fig. 6(a), the peak seen at 1531 cm^{-1} for uncoated-Fe_3O_4PMC is shifted to 1537 cm^{-1} and further to 1539 cm^{-1} for Stöber-Fe_3O_4 PMC and TPRE-Fe_3O_4 PMC samples, respectively [26]. Similar shifts in the peak at 1531 cm^{-1} are observed for the samples with increased OA (oleic acid) coatings, which confirms the decrease in the crystallinity. The positions and intensities of these crystallinity sensitive amide II bands at 1531 cm^{-1} and wider bands from amorphous phases determine the degree of crystallinity [27]. In samples with silica coated MNPs, the silica fingerprint is seen normally around 1700 cm^{-1}, but the nearby corresponding absorbance band appeared as a sharp peak at ca. 1740 and 1742 cm^{-1} for the Stöber-Fe_3O_4 PMC and TPRE-Fe_3O_4 PMC samples, respectively [28]. Also, in the OA samples, the closest absorbance band of OA was observed as a small broad peak in vicinity of 1633 cm^{-1} and around 1716 and 1718 cm^{-1} for 22 w/w% OA-Fe_3O_4 PMC and 55 w/w% OA-Fe_3O_4 PMC samples, respectively [24,29].

The FTIR peaks confirm the synthesis is like that of commercial polyamide 6 (PA6), with the corresponding standard chemical groups [30,31]. As seen in Fig. 6(a), the N-H stretching absorbance band and H-bonding, as observed in PA6, are seen around 3294–3298 cm^{-1}. Major absorbance peaks relating to methylene (CH_2) symmetric and asymmetric stretching vibration bands related to PA6 also appeared around 2860–2866 and 2931–2936 cm^{-1}, and these verify the successful production of PA6 [26,30]. Additionally, these absorbance bands verify the amide II band presence from primary amides, along with the C=O stretching vibration that is attributed to the amide I band functionality. Additional bands relating to amide I and II bands were also seen around 1531–1537 cm^{-1}, being of a primary nature, due to C-N stretching, and further N-H and CO-NH bending [32].

The typical TEM micrographs of the microtome PMC samples show that the MNPs (or agglomerates) dispersion state improves with the silica coating. As observed in Fig. 6(b), (c), (d), (e) and (f), the uncoated-Fe_3O_4 PMC sample, Stöber-Fe_3O_4 PMC sample

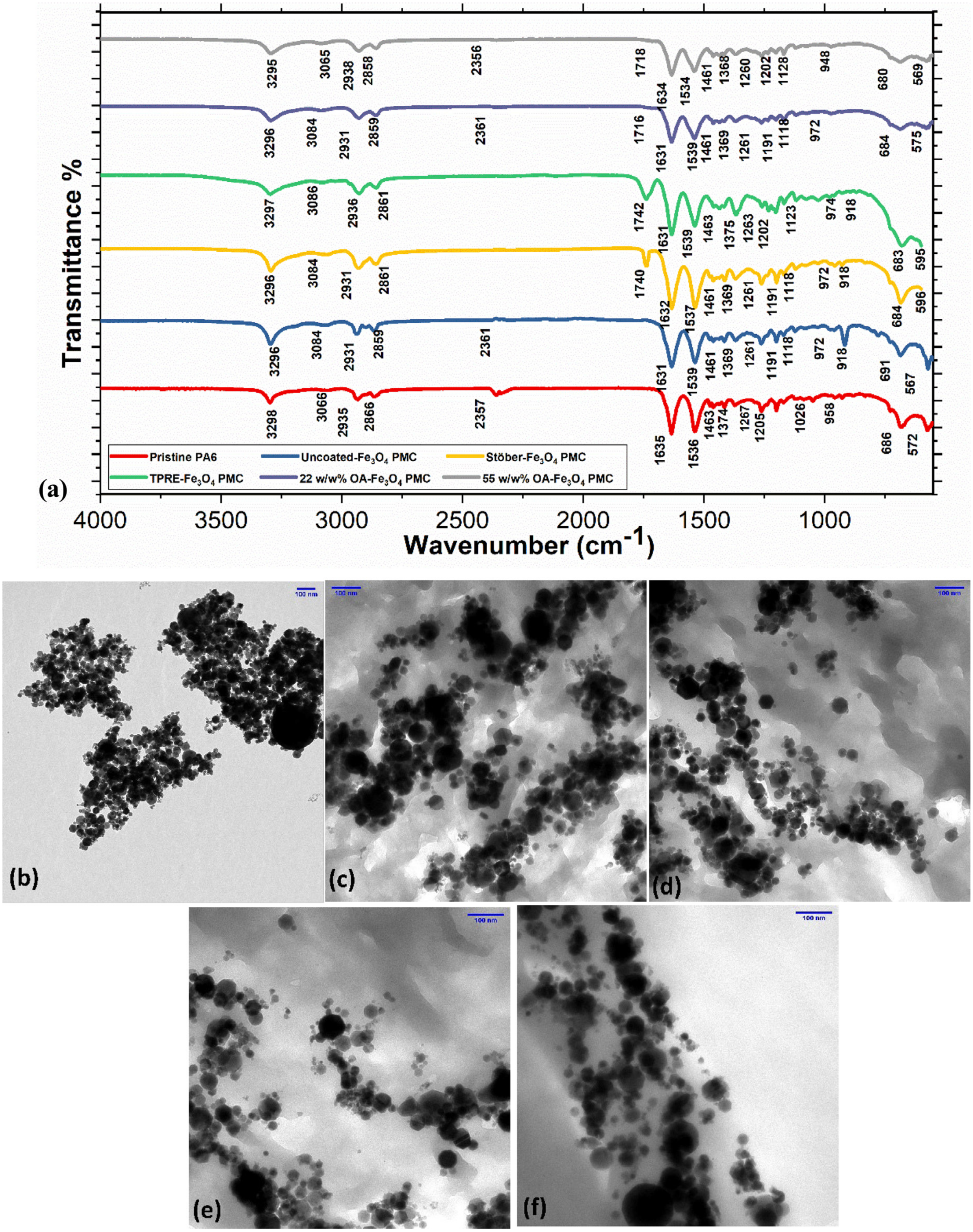

Fig. 6. (a) FTIR spectra of pristine polymer (PA6), sample with uncoated MNPs and samples with varying proportions of silica coatings (Stöber and TPRE) on the MNPs. TEM micrographs showing the dispersion of the nanoparticles in a microtome section of the prepared PMC samples with (b) uncoated MNPs, (c) and (d) MNPs with varying proportions of silica coatings (Stöber and TPRE respectively), and (e) and (f) MNPs with varying proportions of OA coating (22 and 55 w/w% OA respectively) (scale bar shown is of 100 nm).

and 55 w/w% OA-Fe_3O_4 PMC sample formed agglomerates of the MNPs in the PMC due to high dipole–dipole interparticle attraction. However, a uniform dispersion state of the MNPs was observed in both TPRE-Fe_3O_4 PMC and 22 w/w% OA-Fe_3O_4 PMC samples due to the prevalence of the limited interparticle interactions in the presence of the thick silica coating.

3.3. Degree of crystallinity and crystallite size of PMC

The DSC results in Fig. 7(a) exhibit a melting endothermic peak and highlight the glass transition temperatures of all the PMC samples. The peak for the pristine PA6 at *ca.* 46 °C represents the glass transition temperature (T_g), which is in line with the values

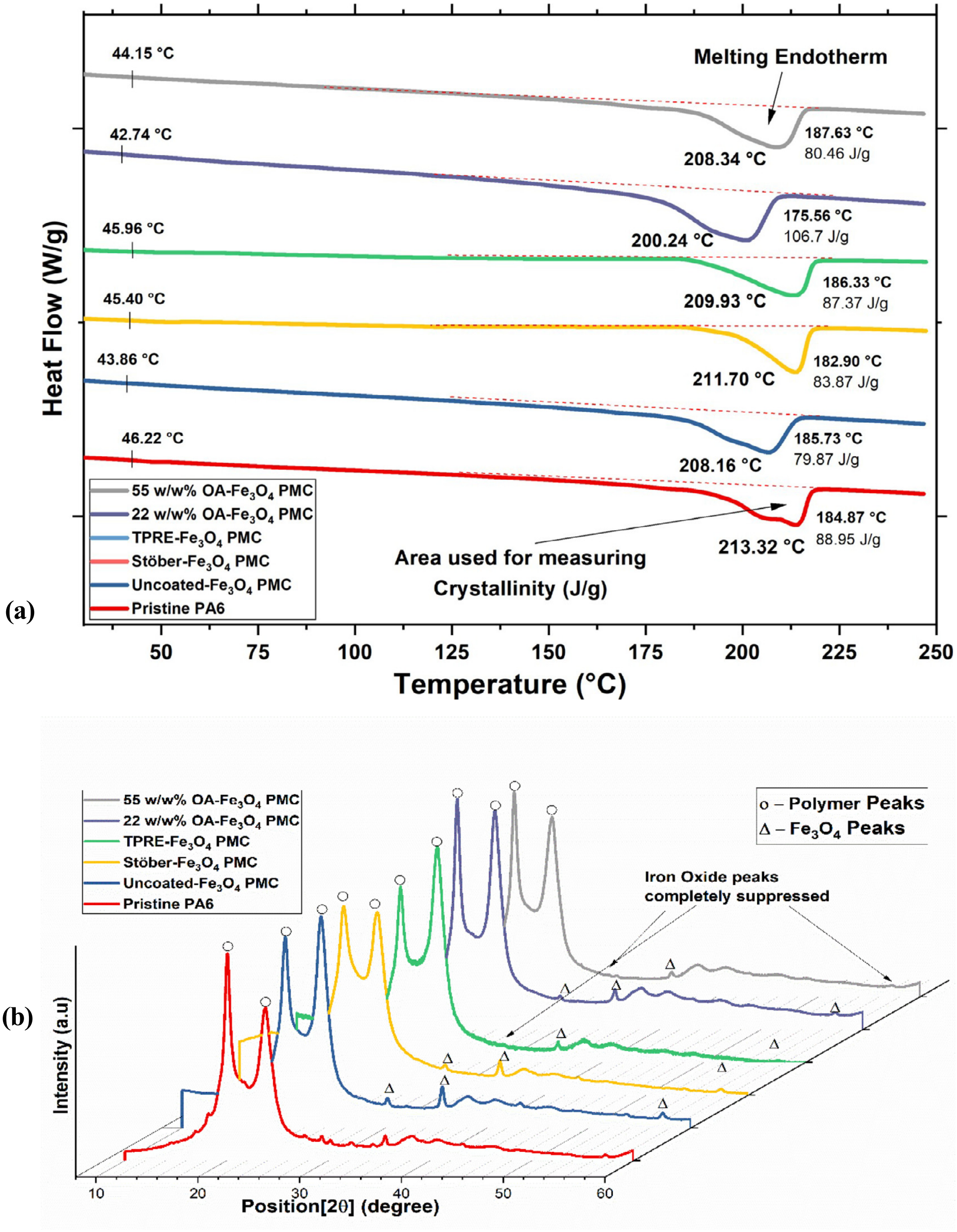

Fig. 7. (a) DSC curves of the pristine PA6 sample, PMC sample with uncoated MNPs, PMC samples with varying proportions of silica coatings (Stöber and TPRE) on the MNPs and PMC samples with varying proportions of OA coatings (22 and 55 w/w%) on the MNPs; (b) XRD patterns of the pristine PA6 sample, PMC sample with uncoated MNPs, PMC samples with varying proportions of silica coatings (Stöber and TPRE) on the MNPs and PMC samples with varying proportions of OA coatings (22 and 55 w/w%) on the MNPs.

reported in the literature [33], though the melting temperature (T_m) of 213.32 °C for PA6 is less than the literature values of 220 °C [33]. Additionally, the T_m and T_g values of the all PMC containing coated MNPs in comparison to uncoated-Fe_3O_4 PMC were found to be higher, but the lowest values of T_m and T_g were recorded for 22 w/w% OA-Fe_3O_4PMC. The values of T_m and T_g are affected by the dispersion state of the particles rather than the type of coating. The increased wetting of the MNPs provides higher crystallisation nucleation sites and improves the crystallinity that results into lower T_m and T_g values. The highest degree of crystallinity amongst all the samples was observed for the 22 w/w% OA-Fe_3O_4 PMC sample, with a value of 56.15%. With no coating on the MNPs' surface, the strong attraction between the MNPs and also with surrounding polymer chains results in a reduction of the cooperative segmental mobility in the polymer and an enhanced T_g value [34–36]. All the observed values and the calculated degree of crystallinity are included in Table S1, Appendix A in the Supporting Data S2.

The crystallinity of the synthesised PMCs was further analysed using XRD results. The major distinctive peaks of the α phase at

Table 2
Estimated Feret diameters of MNPs or their agglomerate regions identified from TEM micrographs, SAXS (Guinier plot) analysis and XRD peak study.

Sample	TEM estimation of MNP/avg. agglomerate size range (nm)		SAXS calculation for MNP/avg. agglomerate size range (nm)	XRD calculation For avg. MNP/agglomerate size range (nm)
	Smallest	Largest		
Uncoated-Fe_3O_4 PMC	25 ± 5	195 ± 10	38 ± 13	42 ± 3
Stöber-Fe_3O_4 PMC	30 ± 5	80 ± 15	32 ± 7	37 ± 5
TPRE-Fe_3O_4 PMC	30 ± 5	60 ± 10	36 ± 6	33 ± 4
22 w/w% OA-Fe_3O_4 PMC	25 ± 5	70 ± 10	31 ± 8	30 ± 3
55 w/w% OA-Fe_3O_4 PMC	25 ± 5	100 ± 10	39 ± 9	42 ± 13

21 and 24°, as seen in Fig. 7(b), match closely with the reference patterns for PA6, whereas the iron oxide peaks in the JCPDS file numbers 82–1533 match with peaks having (hkl) values of (220), (311), (400), (511) and (440) at 2θ values of 30.3, 35.4, 43.1, 57.3 and 62.7°, respectively. The XRD peaks in the XRD patterns of the pristine PA6 are sharper than the peaks of the nanocomposite samples, except for 22 w/w% OA-Fe_3O_4 PMC. The broader XRD peaks can be attributed due to the inclusion of MNPs and overlapping multiple peaks related to non-homogeneous crystallite phases.

The crystalline to amorphous ratios was found to be decreased for Stöber-Fe_3O_4 PMC and TPRE- Fe_3O_4 PMC samples compared to pristine PA6 and uncoated-Fe_3O_4 PMC samples, showing lower crystallinity. Also, the silica-coating may be partially suppressing the MNP (iron oxide) peaks in TPRE-Fe_3O_4 PMC, which otherwise are visible in the XRD patterns of the uncoated-Fe_3O_4 PMC and Stöber-Fe_3O_4 PMC samples. Similarly, the OA coating suppressed the MNP peaks in 55 w/w% OA- Fe_3O_4 PMC, which were otherwise visible in the XRD patterns of 22 w/w% OA-Fe_3O_4 PMC. The XRD peak broadening suggests increase in crystallite size and the crystallite sizes were smaller for all samples except the uncoated-Fe_3O_4 PMC. This again confirmed that the uncoated MNPs are likely to be agglomerated because of dipole–dipole interactions. For the functionalised MNP samples, the low magnetic permittivity silica layer on the MNPs surface may have reduced the MNP-MNP interactions. The summarised observations for all these samples are listed in Table S2, Appendix A in the Supporting Data S2. The calculated values confirmed that 22 w/w% OA-Fe3O4 PMC has the lowest crystallite size.

3.4. Effect of coating on dispersion state of the MNPs

Ensuring a uniform dispersion state of the MNPs within the polymer matrix leads to a high crystallinity PMC with small crystallite sizes and homogeneous magnetic saturations as well as dielectric resistance between the MNPs. Depending upon the chemical composition, molecular structure and thickness of the MNPs surface-coating, dispersions with varying degrees of uniformity, magnetic properties and dielectric properties can result. To determine the effect of the coating on the magnetic properties of PMC, the dispersion state of the MNPs, the magnetic moments of PMC and the polarisation of the PMC were measured and correlated. The agglomerate sizes shown in Table 2 were determined using TEM images, SAXS (Table S3, Appendix A in the Supplementary Data) and XRD calculations (Table S2, Appendix A in the Supplementary Data). These data were utilised as input diameter ranges in the bespoke MATLAB® code [37] to simulate spherical MNPs in the 3D model (Supplementary Data, S5). Firstly, the MNPs dispersion state was evaluated by acquiring TEM images, SAXS/WAXS measurements. TEM micrographs can only be effective in estimating the dispersion state of the MNPs in a few square micrometre areas, however SAXS data have an advantage in evaluating the dispersion state on a bulk scale (ca. volume of few cubed micrometres). The MNP filler structure and polymer chain structures inside a PMC have been previously studied with scattering techniques such as XRD, SAXS/WAXS, etc. [38]. Statistical mechanical theories have related the dispersion state (dictating the space configuration of nano-inclusions, such as the MNPs in PMCs) to stress within the composite [39], and this gives an insight into the effect of the orientations at the nanoscale on the overall mechanical properties at the macro scale. Herein, it also helps in identifying the MNP sizes, including complex agglomerates of MNPs [40] The average diameter derived from the SAXS and XRD analysis are almost identical, as shown in Table 2, though the TEM values are quite varied, especially in the upper range, since it was considered over a broader area in perspective.

This uniform dispersion can lead to a higher degree of the crystallinity phase in the polymer nanocomposite, as will be investigated in the DSC and XRD study of the PMC samples.

3.5. Effect of coating on the polarisation

The polarisation in the network of MNPs also results in dielectric loss and heat dissipation. The P-E measurements were undertaken using the Sawyer-Tower system, with plots shown in Fig. 8. As evidenced in Fig. 8, the 55 w/w% OA-Fe_3 O_4 PMC showed the maximum current leakage as compared to the other PMCs. This lossy system is not ideal for establishing an increased eddy current to help induction heating of the PMC.

The 22 w/w% OA-Fe_3 O_4 PMC had the highest polarisation at 12 kV/mm and the leakage current was also small compared to the other PMCs, which could be desirable for induction heating. The area under the hysteresis represents the leakage current, where a large area represents a high leakage current.

3.6. Combined effect of coating

The electron transfer between nanoparticles depends on the dispersion state of the MNPs in the polymer [41]. In other words, the electromagnetic properties of the synthesised samples must be quantified. An internal radius, IR can be derived by simulating the position of the MNP agglomerates in the matrix of the polymer using a series of TEM images, hence the calculated values of IR represent the dispersion states of the MNPs in the nanocomposites. The simulated modelling of the prepared samples was used to envision and quantify the dispersion state of the uncoated and differently coated MNPs. The interaction radius (IR) of every MNP/agglomerate area was evaluated by the distances between adjacent neighbours (spheres) in the simulated PMC volume.

All the entities were produced as spherical MNP/agglomerate regions to avoid complexity in the simulated model. The simulated PMC sample models (see Supplementary data S5) were generated with 1 wt% of MNPs and are shown in Fig. 9, where small spheres show the individual MNPs or agglomerates and the large spheres particularly show the agglomerates.

In Table 3, the largest agglomerate size of the uncoated-Fe_3O_4 PMC sample also represents the greatest IR value.

The simulated models (Fig. 9(a), (b), (c), (d) and (e) above) represent the dispersion of the MNPs or agglomerates in the

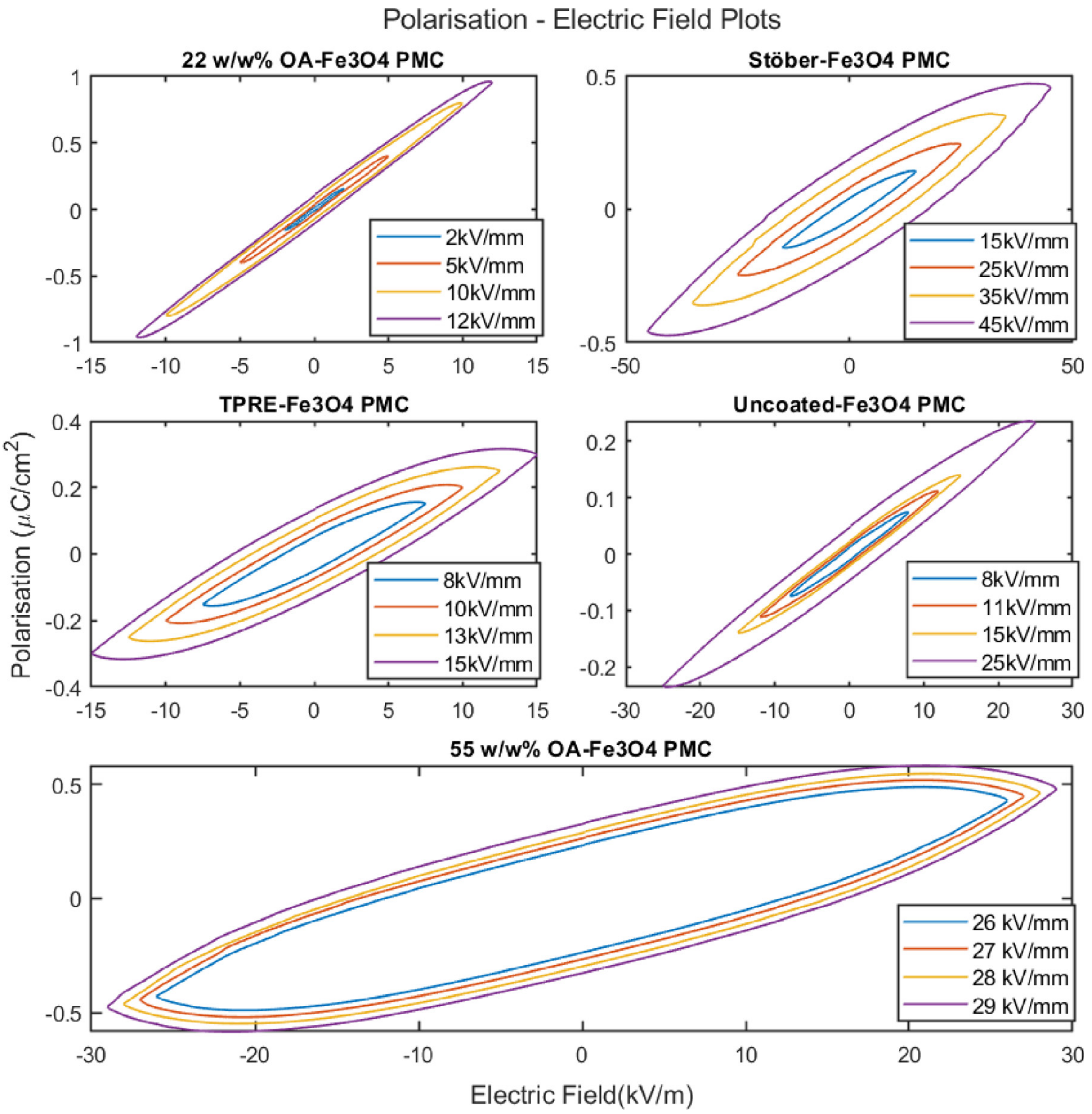

Fig. 8. Polarisation against electric field plots for each sample at different electric field values.

synthesised samples. The IR values of every region, with individual spheres of different sizes (Table 3), aided in determining the influencing region or the interaction region of every MNP in the simulated models. The IR values calculated by the MATLAB® code [42] were used for the graphical representation of the interaction regions, as depicted in Fig. 9(a), (b), (c), (d) and (e), as faint spheres around each solid sphere of the MNP/agglomerate. The changeable IR values, by definition, depend on the MNP sizes as well as the adjacent neighbouring agglomerates, and are found to be between ca. 55 and 475 nm for all the PMC samples simulated. The associated errors with the generated IR values were also calculated as the standard deviation, as summarised in Table 3. Ultimately, this data is related to the calculated magnetic response of all the PMC samples as follows.

According to magnetic (SQUID) measurements at 100 K (Fig. 8(f)), the magnetic moment ratios (Mr/Ms) of 0 for the pristine PA6 sample and 0.46, 0.38, 0.31, 0.32 and 0.57 for the uncoated-Fe3O4 PMC, Stöber-Fe3O4 PMC, TPRE- Fe_3O_4 PMC, 22 w/w% OA-Fe_3O_4 PMC and 55 w/w% OA-Fe_3O_4 PMC samples were obtained, respectively. The measurements taken after increasing the temperature to 400 K (Fig. 9(g)), showed a reduction in the values for the Mr/Ms ratio to 0.30, 0.28, 0.23, 0.24 and 0.31 for uncoated-Fe_3O_4 PMC, Stöber-Fe_3O_4 PMC, TPRE-Fe_3O_4 PMC, 22 w/w% OA-Fe_3O_4 PMC and 55 w/w% OA- Fe_3O_4 PMC. The coercivity for all the PMCs reduced with the increase in temperature [39]. The Mr/Ms ratios below 0.5 for most PMCs indicate the presence of non-interacting single domain MNPs. The coercivity values for all the PMC samples were in the ranges 220–362 and 102–169 Oe at temperatures of 100 and 400 K, respectively. The noted results are summarised in Tables S6 and S7, Appendix A in the Supporting Data S4, respectively.

The onset of crystallisation temperature steadily increased with the increase in silica content, indicating that the MNPs may act as heterogeneous nucleation agents in the PA6 matrix, hence the higher crystallisation rate than that for pristine PA6. Moreover, the decreased melting peak could be attributed to the decreased crystal size observed in the XRD results [43,44]. The DSC and XRD results confirmed that 22 w/w% OA-Fe_3O_4 PMC shows the highest degree of crystallinity and smallest crystallite size, respectively. The key results considered for assessing the appropriate PMC sample with a better overall response are summarised in Table 3.

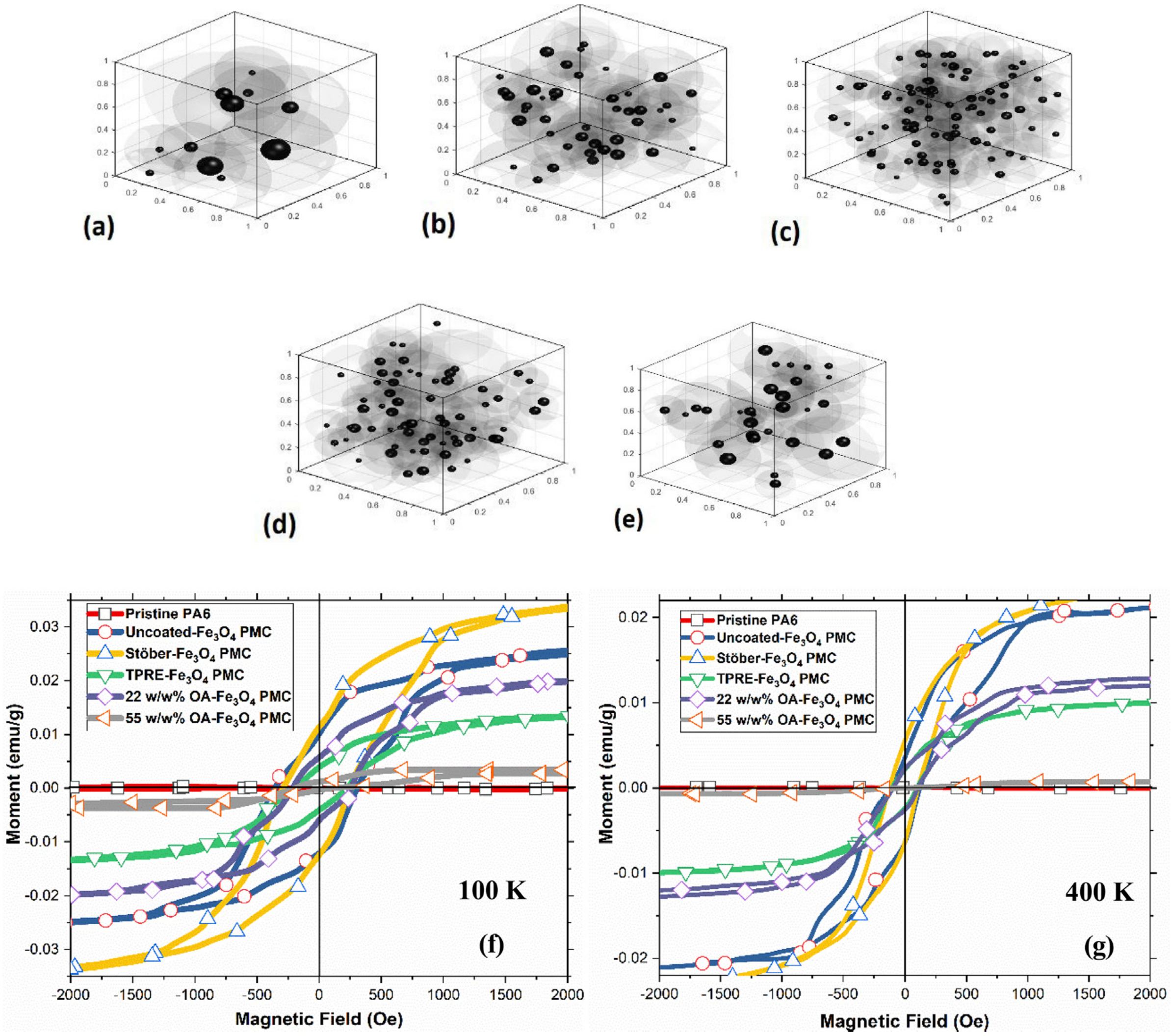

Fig. 9. Simulated model representation of the PMC samples with 1 wt% MNPs and included with the interaction radius (IR) of the individual nanoparticle/agglomerate regions (1 cubic micron size) for (a) uncoated-Fe3O4 PMC and samples with varying proportions of silica coatings i.e. (b) Stöber-Fe3O4 PMC, (c) TPRE-Fe3O4 PMC, (d) 22 w/w% OA-Fe3O4 PMC and (e) 55 w/w% OA-Fe3O4 PMC (herein, solid black spheres represent Fe3O4 MNPs or agglomerates and the faint black region/sphere around it represents their interaction region/range). (f) and (g) Magnetisation hysteresis loops for the pristine PA6 sample, PMC sample with uncoated MNPs, PMC samples with varying percentages of silica coatings (Stöber and TPRE) on the MNPs and PMC samples with varying proportions of OA coatings (22 and 55 w/w%) on the MNPs at 100 and 400 K, respectively.

Similarly, the onset of crystallisation temperature steadily increased with the increase in OA content, again indicating that the MNPs are acting as heterogeneous nucleation agents in the PA6 matrix, hence the higher crystallisation rate than that for pristine PA6. Likewise, the decreased melting peak can be attributed to the decreased crystal size observed in the XRD results [43,44]. The DSC and XRD results confirmed that 22 w/w% OA-Fe_3O_4 PMC showed highest degree of crystallinity and smallest crystallite size, respectively. Additionally, the ferroelectric properties of 22 w/w% OA-Fe_3O_4 PMC were relatively higher than all the other PMC samples. Moreover, with comparatively low Mr/Ms value and a small coercivity value, the hysteresis loop frequency and area under the hysteresis loop could be relatively higher, resulting in efficient heating. As seen in Table 3, 22 w/w% OA-Fe_3O_4 PMC would interact strongly with an external electromagnetic field, complete the eddy current loop, melt at a lower temperature and provide a high degree of crystallinity. The uncoated-Fe_3O_4 PMC sample and Stöber-Fe_3O_4 PMC cannot be chosen, despite their suitably higher magnetic properties, to avoid localised pyrolysis due to the uneven dispersion and agglomeration concerns. Although Stöber-Fe_3O_4 PMC showed almost similar IR values as that of 22 w/w% OA-Fe_3O_4 PMC, it did not perform much better in the other characterisation results, hence it is not a suitable choice. During a cooling–heating cycle through EM stimuli, the interactions between molecules impart the capability of adhesion using directional interactions that dictate the mechanical properties of a material [45], hence the degree of crystallinity, crystallite size and the thermal response of 22 w/w% OA-Fe_3O_4 PMC is more favourable for stimuli application than the other samples. Also, the longer aliphatic coating of OA reduces the cluster stability and hence can result in an increased stimuli response efficiency [45,46]. Due to the inclusion of the magnetisable material Fe_3O_4 in CLm to make PMC, the heat dissipates equivalent to area within the hysteresis loop. However, the amount of power dissipation was low due to the area within the hysteresis of PMC being quite small. Moreover, 22 w/w% OA-Fe_3O_4 PMC, like ferrites, exhibits low saturation magnetisation and permeability, but high polarisability and the ability to establish an electric current loop through percolation at the microscopic level can generate heat at lower frequencies as well as to establish ferromagnetic resonance, helping the heat generation [47]. The other PMCs did not show high polarisability and efficient eddy current loop generation that

Table 3
Summary of key findings from all the characterisation results of the PMC samples.

Sample	Melting temperature Tm (°C)	Degree of crystallinity (%)	Crystallite size (nm)	Magnetic moment ratio (Mr/Ms)	Interaction radius from the simulated model (IR) (nm)	Polarisation (μm/cm^2) @ 12 kV/mm	Key findings
Uncoated-Fe_3O_4 PMC	213.32 ± 2	46.81 ± 2	41.76 ± 4	0.46 ± 0.07 @ 100 K 0.30 ± 0.06 @ 400 K	265 ± 87	0.08	High crystallite size and melting temperature, very low degree of crystallinity and possibility of pyrolysis.
Stöber- Fe_3O_4 PMC	211.70 ± 2	44.14 ± 4	36.47 ± 4	0.38 ± 0.03 @ 100 K 0.28 ± 0.03 @ 400 K	166 ± 58	0.12	Low crystallite size and high melting temperature but lowest degree of crystallinity; lower magnetic response.
TPRE- Fe_3O_4 PMC	209.93 ± 2	45.98 ± 3	33.09 ± 2	0.31 ± 0.05 @ 100 K 0.23 ± 0.04 @ 400 K	129 ± 50	0.31	Low crystallite size but high melting temperature and lower degree of crystallinity; least magnetic response.
22 w/w% OA-Fe_3O_4 PMC	200.24 ± 3	56.15 ± 4	30.02 ± 3	0.32 ± 0.04 @ 100 K 0.24 ± 0.03 @ 400 K	142 ± 52	1	Lowest crystallite size and melting temperature, with highest degree of crystallinity. Least possibility of pyrolysis and maximum magnetic response.
55 w/w% OA-Fe_3O_4 PMC	208.34 ± 2	42.34 ± 2	32.41 ± 13	0.57 ± 0.12 @ 100 K 0.31 ± 0.09 @ 400 K	173 ± 67	0.09	Low crystallite size and degree of crystallinity and high melting temperature. Possibility of pyrolysis and least magnetic response.

can achieve efficient heating [48]. Previously, we have shown the microwave heating of PMC tape [25].

Since both silica and oleic acid have low magnetic permittivity, the thickness of the coating was found to be a sensitive parameter for magnetic saturation of the MNPs. As seen respectively in Tables S4 and S5, Appendix A in the Supporting Data S4, the MNPs with a silica coating (Stöber method) possess the highest magnetic saturation, whereas 55% OA coated MNPs had the lowest value, when considering with the thickness of the coatings (as discussed in Section 3.1, the thickness of coating for Stöber – 2–3 nm, TPRE – 7–9 nm, 22% OA – 2–4 nm and 55% OA – 6–10 nm). However, the magnetic saturation values of the PMC samples were found to be directly proportional to the magnetic saturation values of the MNPs and the IR values. To tune the magnetic and dielectric properties of PMC, it was observed that the coating thickness and dispersion state (IR) of the MNPs within the polymer matrix were required to be adjusted.

Conclusions

This work scrutinises the effect of the coating interface on various properties suitable for self-healing of PA6 polymer magnetic nanocomposites. The effective utilisation of silica and OA as an interface material for coating of Fe_3O_4 MNPs to synthesise the PA6 magnetic polymer nanocomposite (PMC) is proposed to achieve efficient self-healing of the engineering components. The designed PMC was successfully optimised for effective dispersion, dielectric and magnetic properties and it was the 22 w/w% OA sample that was found to be optimal for structural bonding application of the composites, considering all the physical properties, including magnetic and degree/size of crystallinity. With the effect of the 22 w/w% OA coating interface, the magnetic response of the MNPs is not suppressed significantly (second best) and they are able to still give a magnetic moment ratio of 0.32 for the PMC sample. Additionally, the high polarisability of the 22 w/w% OA PMC helps establishing resonance and eddy currents, and its conductive properties helps with efficient heating. Although not the highest amongst all the samples, it showed the highest degree of crystallinity at 56.15% with an interaction radius of 142 nm, making it the most suitable candidate for EM stimuli application.

CRediT authorship contribution statement

Ranjeetkumar Gupta: Investigation, Visualization, Data collating, Plotting, Writing – original draft. **Pinakin V. Pancholi:** Advising, Concept correction, Reviewing. **Xiangyan Yu:** PE plots and measurements, Plotting, Data collection. **Gavin B.G. Stenning:** Overseeing magnetic characterisation, Data collection, Reviewing. **David Bucknall:** Reviewing & useful discussions. **David Flynn:** Reviewing & useful discussions. **Ketan Pancholi:** Conceptualization, Methodology, Experimental protocols, Project management, Supervision, Writing – review & editing.

Declaration of competing interest

The authors declare the following financial interests/personal relationships which may be considered as potential competing interests: Ketan Pancholi reports financial support and article publishing charges were provided by Robert Gordon University. Ketan Pancholi reports equipment, drugs, or supplies was provided by Rutherford Appleton Laboratory.

Data availability

Data will be povided upon request.

Acknowledgements

Ranjeet thanks Robert Gordon University, United Kingdom for his Ph.D. studentship funding. The authors are grateful to the School of Pharmacy at Robert Gordon University for making their facility available for part of this research.

Appendix A. Supplementary data

Supplementary material related to this article can be found online at https://doi.org/10.1016/j.nanoso.2023.100973.

References

[1] D. Flynn, N.S. Sudan, A. Toon, M.P.Y. Desmulliez, Fabrication process of a micro-inductor utilising a magnetic thin film core, Microsyst. Technol. 12 (10–11) (2006) 923–933;
V. Mittal, Barrier resistance generation in polymer nanocomposites, in: Optimization of Polymer Nanocomposite Properties, 2010, pp. 1–19.

[2] Y. Li, J. Zhu, S. Wei, J. Ryu, Q. Wang, L. Sun, Z. Guo, Poly (propylene) nanocomposites containing various carbon nanostructures, Macromol. Chem. Phys. 212 (2011) 2429–2438.

[3] G. Ariu, Functionalised Graded Composites for Induction Processing in Manufacture (Doctoral dissertation), University of Bristol, 2019.

[4] T. Bayerl, M. Duhovic, P. Mitschang, D. Bhattacharyya, The heating of polymer composites by electromagnetic induction–A review, Composites A 57 (2014) 27–40.

[5] T. Bayerl, R. Schledjewski, P. Mitschang, Induction heating of thermoplastic materials by particulate heating promoters, Polym. Polym. Compos. 20 (4) (2012) 333–342.

[6] A. Riccio, A. Russo, P. Raimondo, A. Cirillo, A. Caraviello, A numerical/experimental study on the induction heating of adhesives for composite materials bonding, Mater. Today Commun. 15 (2018) 203–213.

[7] J. Fiabane, P. Prentice, K. Pancholi, High yielding microbubble production method, BioMed Res. Int. (2016).

[8] C.B. Roth, J.R. Dutcher, Glass transition and chain mobility in thin polymer films, J. Electroanal. Chem. 584 (2005) 13–22.

[9] A.S. Ahmed, R.V. Ramanujan, Curie temperature controlled self-healing magnet–polymer composites, J. Mater. Res. 30 (2015) 946–958.

[10] R. Vijayaákumar, Y. Koltypin, Y.S. Cohen, Y. Cohen, D. Aurbach, O. Palchik, I. Felner, A. Gedanken, Preparation of amorphous magnetite nanoparticles embedded in polyvinyl alcohol using ultrasound radiation, J. Mater. Chem. 10 (2000) 1125–1129.

[11] S. Park, N. Bernet, S. De La Roche, H. Hahn, Processing of iron oxide-epoxy vinyl ester nanocomposites, J. Compos. Mater. 37 (2003) 465–476.

[12] M. Hetti, W.C. Lai, C.W. Tse, C.K. Cheung, Y.F. Lee, Y.M. Lai, W.Y. Kung, Release film with enhanced mechanical properties and method in preparing thereof, 2015, U.S. Patent Application No. 14/063, 465.

[13] Y. Chen, A.M. Kushner, G.A. Williams, Z. Guan, Multiphase design of autonomic self-healing thermoplastic elastomers, Nature Chem. 4 (2012) 467–472.

[14] Y. Chen, S. Zhou, H. Yang, L. Wu, Structure and properties of polyurethane/nanosilica composites, J. Appl. Polym. Sci. 95 (2005) 1032–1039.

[15] J. Tang, Y. Wang, H. Liu, Y. Xia, B. Schneider, Effect of processing on morphological structure of polyacrylonitrile matrix nano-ZnO composites, J. Appl. Polym. Sci. 90 (2003) 1053–1057.

[16] D. Ma, T.A. Hugener, R.W. Siegel, A. Christerson, E. Mårtensson, C. Önneby, L.S. Schadler, Influence of nanoparticle surface modification on the electrical behaviour of polyethylene nanocomposites, Nanotechnology 16 (2005) 724.

[17] A. Usuki, M. Kawasumi, Y. Kojima, A. Okada, T. Kurauchi, Synthesis and properties of diamine- modified nylon 6-clay hybrid, Kobunshi Ronbunshu (Tokyo) 52 (1995) 440–444.

[18] Z. Spitalsky, G. Tsoukleri, D. Tasis, C. Krontiras, S. Georga, C. Galiotis, High volume fraction carbon nanotube–epoxy composites, Nanotechnology 20 (2009) 405702.

[19] M. Zahn, Electromagnetic Field Theory: A Problem Solving Approach, 1979.

[20] S. Campelj, D. Makovec, M. Drofenik, Preparation and properties of water-based magnetic fluids, J. Phys.: Condens. Matter 20 (2008) 204101.

[21] K.R. Iler, The Chemistry of Silica. Solubility, Polymerization, Colloid and Surface Properties and Biochemistry of Silica, 1979.

[22] W. Stöber, A. Fink, E. Bohn, Controlled growth of monodisperse silica spheres in the micron size range, J. Colloid Interface Sci. 26 (1968) 62–69.

[23] R. Gupta, R. Staknevicius, K. Pancholi, Rapid multifunctional composite part manufacturing using controlled in-situ polymerization of PA6 nanocomposite, Procedia CIRP 85 (2019) 61–65, http://dx.doi.org/10.1016/j.procir.2019.10.003.

[24] R. Gupta, K. Pancholi, S. Rulston De, D. Murray, D. Huo, G. Droubi, M. White, J. Njuguna, Effect of oleic acid functionalised iron oxide nanoparticles on properties of magnetic polyamide-6 nanocomposite, JOM 71 (2019) 3119–3128, http://dx.doi.org/10.1007/s11837-019-03622-5.

[25] R. Gupta, D. Huo, M. White, V. Jha, G.B. Stenning, K. Pancholi, Novel method of healing the fibre reinforced thermoplastic composite: A potential model for offshore applications, Compos. Commun. 16 (2019) 67–78.

[26] N. Ngwuluka, Application of in situ polymerization for design and development of oral drug delivery systems, Aaps Pharmscitech 11 (2010) 1603–1611.

[27] F. Yang, M. Zhao, B. Zheng, D. Xiao, L. Wu, Y. Guo, Influence of pH on the fluorescence properties of graphene quantum dots using ozonation pre-oxide hydrothermal synthesis, J. Mater. Chem. 22 (2012) 25471–25479.

[28] P. Larkin, IR and Raman spectra—Structure correlations: Characteristic group frequencies, Infrared Raman Spectrosc. (2011) 73–115.

[29] D. Tunc, H. Bouchekif, B. Améduri, C. Jérôme, P. Desbois, P. Lecomte, S. Carlotti, Synthesis of aliphatic polyamide bearing fluorinated groups from ε-caprolactam and modified cyclic lysine, Eur. Polym. J. 71 (2015) 575–584.

[30] G. Xu, W. Lu, X. Feng, S. Yu, Self-assembly of organic–inorganic nanocomposites with nacre-like hierarchical structures, Soft Matter 7 (2011) 4828–4832.

[31] R. Gupta, K. Pancholi, R. Prabhu, M. Pancholi, D. Huo, V. Jha, J. Latto, Integrated self-healing of the composite offshore structures, in: OCEANS 2017-Aberdeen, 2017, pp. 1–4.

[32] J. Pockett, Crystallinity in Linear Polyamides: A Study using Melt Blending with Small-Molecule Diluents, University of South Australia, 2004.

[33] C. Scott, Nylon-6 information and properties, 2019, http://www.polymerprocessing.com/polymers/PA6.html (accessed February/20, 2019).

[34] P. Rittigstein, J.M. Torkelson, Polymer–nanoparticle interfacial interactions in polymer nanocomposites: confinement effects on glass transition temperature and suppression of physical aging, J. Polym. Sci. B 44 (2006) 2935–2943.

[35] F. Rybnikář, P. Geil, Melting and recrystallization of PA-6/PA-66 blends, J. Appl. Polym. Sci. 49 (1993) 1175–1188.

[36] S. Pashaei, M.M. Avval, A.A. Syed, Thermal degradation kinetics of nylon6/GF/crysnano nanoclay nanocomposites by TGA, Chem. Ind. Chem. Eng. 17 (2011) 141–151.

[37] R. Gupta, L. Smith, J. Njuguna, A. Deighton, K. Pancholi, Insulating MgO-Al2O3-LDPE nanocomposites for offshore medium voltage DC cable, ACS Appl. Electron. Mater. 2 (2020) 1880–1891, http://dx.doi.org/10.1021/acsaelm.0c00052.

[38] S. Thomas, D. Rouxel, D. Ponnamma, Spectroscopy of Polymer Nanocomposites, William Andrew, 2016.

[39] R. Gupta, P. Gupta, C. Footer, et al., Tuneable magnetic nanocomposites for remote self-healing, Sci. Rep. 12 (2022) 10180, http://dx.doi.org/10.1038/s41598-022-14135-8.

[40] J. Teixeira, Small-angle scattering by fractal systems, J. Appl. Crystallogr. 21 (1988) 781–785.

[41] L. Pallon, A. Hoang, A. Pourrahimi, M.S. Hedenqvist, F. Nilsson, S. Gubanski, U. Gedde, R.T. Olsson, The impact of MgO nanoparticle interface in ultra-insulating polyethylene nanocomposites for high voltage DC cables, J. Mater. Chem. A 4 (2016) 8590–8601.

[42] R. Gupta, B. Badel, P. Gupta, D.G. Bucknall, D. Flynn, K. Pancholi, Flexible low-density polyethylene–BaTiO3 nanoparticle composites for monitoring leakage current in high-tension equipment, ACS Appl. Nano Mater. 4 (2021) 2413–2422.

[43] A. Rajan, M. Sharma, N.K. Sahu, Assessing magnetic and inductive thermal properties of various surfactants functionalised Fe3O4 nanoparticles for hyperthermia, Sci. Rep. 10 (1) (2020) 1–15.

[44] J. Cho, D. Paul, Nylon 6 nanocomposites by melt compounding, Polymer 42 (2001) 1083–1094.

[45] A. Rajan, M. Sharma, N.K. Sahu, Assessing magnetic and inductive thermal properties of various surfactants functionalised Fe_3O_4 nanoparticles for hyperthermia, Sci. Rep. 10 (1) (2020) 15045.

[46] G. Jimenez, N. Ogata, H. Kawai, T. Ogihara, Structure and thermal/mechanical properties of poly (ϵ-caprolactone)-clay blend, J. Appl. Polym. Sci. 64 (1997) 2211–2220.

[47] K. Mphahlele, S.S. Ray, A. Kolesnikov, Self-healing polymeric composite material design, failure analysis and future outlook: a review, Polymers 9 (2017) 535.

[48] L. Guadagno, M. Raimondo, C. Naddeo, P. Longo, A. Mariconda, W.H. Binder, Healing efficiency and dynamic mechanical properties of self-healing epoxy systems, Smart Mater. Struct. 23 (2014) 045001.